

***Investigation of the PSE approach for
subsonic and supersonic hot jets.
Detailed comparisons with LES and
Linearized Euler Equations results***

by

**Estelle Piot, Gregoire Casalis,
Frederic Muller and Christophe Bailly**

reprinted from

international journal of

aeroacoustics

volume 5 · number 4 · 2006

published by MULTI-SCIENCE PUBLISHING CO. LTD.,

5 Wates Way, Brentwood, Essex, CM15 9TB UK

E-MAIL: mscience@globalnet.co.uk

WEBSITE: www.multi-science.co.uk

Investigation of the PSE approach for subsonic and supersonic hot jets. Detailed comparisons with LES and Linearized Euler Equations results

**Estelle Piot^{*}, Gregoire Casalis[†],
Frederic Muller[‡] and Christophe Bailly[§]**

^{}†ONERA DMAE, 2 av. Ed. Belin, BP. 4025, 31 055 Toulouse Cedex, France*

^{}PhD student, estelle.piot@oncert.fr, [†]Research Engineer, gregoire.casalis@oncert.fr*

[‡]ONERA DSNA, 29 av. D. Leclerc, 92322 Châtillon Cedex, France

PhD student, frederic.muller@onera.fr

[§]Ecole Centrale Lyon, 36 avenue Guy de Collongue, 69134 Ecully Cedex, FRANCE

Professor, christophe.bailly@ec-lyon.fr

ABSTRACT

A Parabolized Stability Equation (PSE) method is applied to hot inviscid Mach 0.7 and Mach 2 axisymmetric jets. The Parabolized Stability Equations are derived from the linearized Euler equations. Spatial development of pressure perturbations is computed in the vicinity of the jet, and the associated radiated noise is obtained by solving the wave equation. A Large Eddy Simulation is performed on the subsonic jet and compared with the results obtained by the PSE analysis of the LES-computed mean flow. Good agreement is found for the spatial growth of pressure instability waves, the spatial damping being slightly under-estimated in the PSE analysis. Only LES predicts acoustic radiation, which may thus be created by the turbulence cascade rather than by the Kelvin-Helmholtz instability waves. PSE method is then applied to the supersonic jet and compared to solutions of Linearized Euler Equations. The common mean flow is analytical. A very good agreement is found for pressure perturbation evolution and for directivity and levels of acoustic radiation.

1. INTRODUCTION

Over the past 30 years, jet noise has been the subject of many experiments and many theoretical models have been tested to understand the physics of the phenomenon. However despite all these studies and despite the apparent simplicity of a jet, it is still very difficult to correctly predict a jet noise radiation. It is now generally accepted that jet noise is created by both fine and large-scale turbulence structures (Tam 1995). The dominant part of subsonic jet noise is produced by fine-scale turbulence, whereas large

turbulence structures are dominant noise sources of supersonic and high temperature jets. For imperfectly expanded supersonic jets, additional noise is created by shock cell structures which are formed in the jet plume. One part of this noise is called screech tones noise, the other broadband shock-associated noise. Tam et al. (1996, 1994) showed that for both subsonic and supersonic jets, large turbulence structures generate noise. Since the work of Tam & Burton (1984), it is known that these structures are in fact instability waves, which radiate sound when they propagate downstream at supersonic speed relative to ambient conditions. Tam and Burton developed a matching asymptotic expansion method to calculate the noise radiation in the far-field. To calculate the instability wave evolution, several methods were developed, especially the classical locally parallel-flow stability theory or the multiple scales method which takes into account the slowly divergence of the jet flow (Crighton & Gaster 1976, Saric 1975, Morris 1981).

In this work, the Parabolized Stability Equations (PSE) will be used to calculate the instability waves. The PSE formulation was first introduced by Herbert & Bertolotti (Herbert & Bertolotti 1987, Herbert 1991, Herbert 1993) to study the streamwise evolution of single or interacting instability modes in boundary layers. This approach is based upon the decomposition of each mode into a slowly varying amplitude function and a wave function with a slowly varying wavenumber. The decomposition is introduced into the linearized Navier-Stokes equations, which are then parabolized by neglecting some terms. Yen and Messersmith successfully applied this PSE approach to the prediction of jet instabilities in both an incompressible (1998) and compressible (1999) jet. Malik & Chang (1997 and 2000) studied a cold Mach 2.5 supersonic laminar jet, with both linear and non-linear PSE. Balakumar (1998) performed on a cold Mach 2.1 supersonic high Reynolds number jet a linear PSE calculation coupled with a solution of the wave equation in the far-field; he found good agreement between his acoustic prediction and previous experimental measurements. More recently, Lin et al. (2004) applied PSE analysis on a high Reynolds number Mach 0.9 heated jet. They solved the wave equation to compute the acoustic field, and obtained good prediction of the aft angle jet noise radiation. Bertolotti & Colonius (2003) discovered also in a heated Mach 0.9 jet so called "core modes" which travel supersonically within the jet potential core. In all these studies, comparisons have only been made with experimental acoustic measurements. But other methods exist to predict noise radiation, especially high-fidelity numerical simulations such as Direct Numerical Simulation (DNS) (Mitchell et al. 1999), Large Eddy Simulation (LES) (Andersson et al. 2005), or methods which solve directly the linearized Navier-Stokes (Mosheni et al. 2002) or linearized Euler equations (Mankbadi et al. 1998). Some studies compare PSE results with results from these methods, especially Cheung & Lele (2004) and Day et al. (2001), who compare PSE calculations with DNS results. They can then not only compare acoustic pressure radiation, but also pressure eigenfunctions in the near-field. But these comparisons are made for mixing layers, and at low Reynolds numbers, because of the computational cost of DNS.

In this paper a Mach 0.7 subsonic jet and a Mach 2 supersonic jet are considered. Both are hot high-Reynolds number turbulent axisymmetric jets. On the subsonic jet a

Large-Eddy Simulation is performed, and the Linearized Euler Equations are solved for the supersonic jet. We study for both jets the streamwise growth of a linear Kelvin-Helmholtz instability wave by solving the associated Parabolized Stability Equations, which are derived from the Euler equations. On the contrary, above-mentioned PSE studies on high-Reynolds number jets use equations derived from the complete viscous Navier-Stokes equations, but in which the Reynolds number is fixed at a large value. The acoustic pressure in the far field is also calculated by solving the wave equation with the pressure obtained from the PSE as the inner boundary data. For both jets pressure evolution obtained by the PSE computations is compared to the Large-Eddy Simulation or Linearized Euler Equations results.

The objective of this paper is to determine whether the Euler-based PSE equations are valid and whether their both near-field and acoustic pressure evolution prediction compares well to the Large Eddy Simulation or Linearized Euler Equations results, not only in the region where the mean flow is unstable, but also in the stable region. We first give a detailed description of the PSE method based on Euler equations, and of acoustic calculation; the numerical implementation is explained, and the code is validated against previous published results and classical locally parallel-flow stability method. Then the method is applied to a subsonic hot jet, and compared to a LES simulation of the same jet flow. Finally comparisons of the PSE-computed near-field and acoustic pressure with Linearized Euler Equations solution on a supersonic hot jet are discussed.

2. PARABOLIC STABILITY EQUATIONS FOR COMPRESSIBLE INVISCID FLOW

2.1 The linearized Euler equations

In the present study, an inviscid jet flow is considered, and the cylindrical coordinate system is used, (r, θ, x) denoting radial, azimuthal, and streamwise directions respectively. The evolution of the flow field is governed by the Euler equations written for a compressible gas :

$$\left\{ \begin{array}{l} \frac{\partial \rho}{\partial t} + \underline{\nabla} \rho \cdot \mathbf{u} + \rho \underline{\nabla} \cdot \mathbf{u} = 0 \\ \frac{\partial \mathbf{u}}{\partial t} + \underline{\nabla} \mathbf{u} \cdot \mathbf{u} = -\frac{1}{\rho} \underline{\nabla} p \\ \frac{\partial S}{\partial t} + \underline{\nabla} S \cdot \mathbf{u} = 0 \end{array} \right. \quad (1)$$

where $\mathbf{u} = (u_r, u_\theta, u_x)$ is the velocity vector, ρ the density, p the pressure, S the entropy and t the time. Using the perfect gas assumption, the entropy is thus given by $S = C_v \ln p/\rho^\gamma$, the specific heat capacity at constant volume C_v and the specific heat ratio γ being constant. The convention whereby subscript “j” refers to the conditions at the jet exit is used, and the lengths are non-dimensionalized by the diameter D_j , the velocity by the

streamwise exit velocity u_j , the density by ρ_j , the pressure by $\rho_j u_j^2$, the time by D_j/u_j , and other variables by the corresponding jet exit conditions. For reading easiness, the dimensionless Euler equations are written with the same notations as in Eqn (1).

We are concerned with the spatial evolution of a small perturbation inside the jet flow. The linear stability analysis consists in decomposing the instantaneous value of any variable q into a mean value \bar{q} and a small perturbation quantity \tilde{q} :

$$\mathbf{u} = \bar{\mathbf{u}} + \tilde{\mathbf{u}}, \quad p = \bar{p} + \tilde{p}, \quad \rho = \bar{\rho} + \tilde{\rho}, \quad S = \bar{s} + \tilde{s} \quad (2)$$

The basic flow is assumed known, is steady and axisymmetric (independent of the azimuthal angle θ , and without azimuthal component). Moreover the non-dimensional mean pressure is assumed uniform in the solution domain, and is equal to $1/(\gamma M_j^2)$ with the scaling used in this paper.

Substituting Eqn (2) into Eqn (1), and subtracting from it the steady mean flow equations, the linear disturbance equations can be expressed in the form :

$$A\phi + B\frac{\partial\phi}{\partial x} + C\frac{\partial\phi}{\partial r} + D\frac{\partial\phi}{\partial\theta} + E\frac{\partial\phi}{\partial t} = 0 \quad (3)$$

where ϕ is the perturbation vector :

$$\phi = (\tilde{u}_r, \tilde{u}_\theta, \tilde{u}_x, \tilde{\rho}, \tilde{p})^T.$$

Equation (3) remains valid as long as the fluctuating quantities amplitudes are small in comparison with the corresponding basic flow amplitudes. Matrices A , B , C , D , and E are composed of mean flow quantities, which are functions of the coordinates r and x only.

2.2 Conventional stability approach

The conventional stability theory has been used for axisymmetric jet flows for several years, e.g. Michalke (1984) and Tam & Burton (1984) or more recently Millet & Casalis (2002). This theory is usually called “linear parallel stability theory”, because the basic flow is there considered as being locally parallel. This means that the mean quantities are supposed to be r -dependent only, and that the mean radial velocity is neglected. Therefore, when Eqn (3) is written at a specific streamwise location x , the matrices are independent of x , θ , and t . The disturbance quantities can then be written in the normal mode form:

$$\tilde{q}(r, \theta, x, t) = \hat{q}(r) \exp(i(kx + m\theta - \omega t)) \quad (4)$$

where ω is the frequency of the disturbance, k and m are the streamwise and azimuthal wavenumbers, respectively. Here i stands for the square root of -1 . Whereas ω and m are real numbers, k is a complex number, whose imaginary part stands for the opposite of the spatial growth rate of the disturbance.

As the amplitude function \hat{q} is a function of r only, when Eqn (4) is substituted in the linearized Euler equations (3), an ordinary differential equation for $\hat{q}(r)$ is obtained.

Associated to homogeneous boundary conditions (Tam & Burton, 1984), this system corresponds to an eigenvalue problem with streamwise wavenumber k as the eigenvalue and $\hat{q}(r)$ as the associated eigenfunction. This problem can thus be solved at each chosen axial location, in a easy way as long as the spatial growth rate of the disturbance is positive. But when the disturbance is spatially damped, the numerical computation becomes difficult. Indeed, as explained by Tam & Burton (1984) or Michalke (1984) for instance, the problem can then only be solved by extending the ordinary differential equation into the complex plane : the equation, initially written with the real coordinate r , is then written with a complex coordinate, which creates several technical difficulties. Moreover, because of this extension, it becomes impossible to catch directly the physical fluctuating amplitudes $\hat{q}(r)$ in the damped region.

2.3 Parabolized stability equations

For most of the practical applications, the mean flow varies slowly in the streamwise direction. The idea of the Parabolized Stability Equations (PSE) approach, initially developed by Herbert & Bertolotti (Herbert & Bertolotti 1987, Herbert 1991, Bertolotti et al. 1992), is to take into account the non-parallelism of the flow by decomposing the x -dependent terms of the disturbance quantities into a slowly varying shape (amplitude) function and a rapidly wave-like part to obtain

$$\tilde{q}(r, \theta, x, t) = \hat{q}(r, x) \exp\left(i \int_{x_0}^x \alpha(\xi) d\xi\right) \exp(i(m\theta - \omega t)) \quad (5)$$

In this generalized normal mode form $\hat{q}(r, x)$ is the slowly varying shape function, α the complex streamwise wavenumber, and the azimuthal wavenumber m and the disturbance frequency ω are constant real numbers, as for the local conventional stability approach. x_0 is the minimum streamwise value of the computational domain. An analysis of Eqn (5) reveals that the streamwise change of the disturbance can be absorbed into either the shape function or the exponential term containing the streamwise wavenumber. This ambiguity must be resolved through the introduction of an additional equation, which imposes a condition on the shape function such that most of the waviness and growth of the disturbance are absorbed into the exponential term, making the shape function $\hat{q}(r, x)$ slowly varying in x , and thus determining the value of the streamwise wavenumber α .

The additional equation proposed by Herbert & Bertolotti (Herbert & Bertolotti 1987) is called a normalization and consists in setting to zero the x -derivative of a given integral norm, for example the norm based on the kinetic energy of the shape function. The normalization based on this norm is then:

$$\int_0^{+\infty} \left(\hat{u}_r^* \frac{\partial \hat{u}_r}{\partial x} + \hat{u}_\theta^* \frac{\partial \hat{u}_\theta}{\partial x} + \hat{u}_x^* \frac{\partial \hat{u}_x}{\partial x} \right) dr = 0 \quad \forall x \quad (6)$$

where * denotes complex conjugate. The choice of another specific normalization would change the computed values of α and $\hat{q}(r, x)$, but not the value of the physical disturbance $\tilde{q}(r, \theta, x, t)$, as explained by Herbert (1993). This is numerically proved in a following section.

Substituting Eqn (5) into Eqn (3), the parabolized stability equation is obtained:

$$\hat{A}\hat{\phi} + \hat{B}\frac{\partial\hat{\phi}}{\partial x} + \hat{C}\frac{\partial\hat{\phi}}{\partial r} = 0 \quad (7)$$

where the (5×5) matrices \hat{A} , \hat{B} , and \hat{C} are explicitly given in appendix. They are functions of the mean flow and its derivatives, and of ω , m , and α . The shape function vector $\hat{\phi}$ is:

$$\hat{\phi} = (\hat{u}_r, \hat{u}_\theta, \hat{u}_x, \hat{\rho}, \hat{p})^T. \quad (8)$$

Equation (7) is a partial differential equation with respect to r and x . Indeed, the mean flow is assumed to be weakly non-parallel, i.e. the mean flow variables are functions of r and x , the mean radial velocity being small. Moreover, the streamwise slowly varying assumption implies that all the x -derivatives of variables are small, and that the term $\partial^2\hat{q}/\partial x^2$ is negligible. This property is used to justify the parabolicity for the Navier-Stokes equations based problem. However, as an inviscid flow is considered, the latter term never appears in our equation. A standard analysis of the mathematical nature of Eqn (7) shows that a sufficient condition to be parabolic is that:

$$\forall x, \forall r, \quad M_j^2 \bar{\rho}(r, x) (\bar{u}_x(r, x))^2 < 1 \quad (9)$$

Whenever this condition is satisfied we can then claim that Eqn (7) is a parabolic stability equation rather than a parabolized one. However we will still call Eqn (7) the ‘‘PSE’’ equation.

At $r = 0$, since some terms in the PSE equation are singular the following boundary conditions are used:

$$\begin{aligned} \forall x, \quad \hat{u}_r(0, x) = 0 & \quad \text{for } m = 0 \\ \hat{u}_r(0, x) + im\hat{u}_\theta(0, x) = 0, \quad \hat{p}(0, x) = 0 & \quad \text{for } m \geq 1 \end{aligned} \quad (10)$$

They are completed by the non-singular terms in the PSE equations, expressed at $r = 0$. In the far field $r \rightarrow +\infty$, the mean flow is uniform : $\bar{u}_r = \bar{u}_x = \bar{u}_\theta = 0$, and $\bar{\rho} = \rho_\infty$. Neglecting all the derivatives in the streamwise direction, and after some substitutions, Eqn (7) reduces to :

$$\frac{\partial^2 \hat{p}}{\partial r^2} + \frac{1}{r} \frac{\partial \hat{p}}{\partial r} + \left(\rho_\infty \omega^2 M^2 - \frac{m^2}{r^2} - \alpha^2 \right) \hat{p} = 0 \quad (11)$$

The other shape functions are proportional to \hat{p} or $\partial\hat{p}/\partial r$. Therefore in the far field the pressure shape function takes the form of a Hankel function of the first kind and order m :

$$\hat{p}(r, x) = H_m^1(ir\lambda(x)) \quad (12)$$

where $\lambda(x)$ is the positive square root of $\alpha^2(x) - \rho_\infty w^2 M_j^2$.

These Hankel-based boundary conditions are very accurate, though they do not consider the non-parallelism of the problem. Moreover, they are valid as soon as the mean flow becomes uniform. In the present computations, these boundary conditions are imposed farther, at $r \sim 10D_j$.

If criterion (9) is satisfied, the PSE equation (7) is parabolic; a normalization is mandatory but could be an arbitrary one. However the choice of the boundary conditions Eqn (12) explains why the normalization given by Eqn (6) must be used. Indeed, this normalization imposes that the exponential term of Eqn (5) controls the waviness and growth of the disturbance, as it happens in the conventional parallel approach. For the PSE computations the Hankel-based boundary conditions which assumes a basic parallel flow are used. Consequently the PSE solution must be close to the conventional parallel solution; this is forced by normalization Eqn (6).

2.4 Numerical techniques

The parabolicity of the governing equation (7) is the major advantage of the PSE formulation.

Indeed, this permits to find the solution of the problem by a marching procedure in the x direction. To compute the solution, we need to discretize the equations in both x and r directions. The radial grid is partitioned into two domains, to obtain a good accuracy around the location where the mean streamwise velocity presents an inflection point. The interface between the two domains occurs just outside the lip-line of the jet, at $r/D_j = 0.506$. A crucial aspect of this decomposition is the manner in which solutions on contiguous domains are matched. To get good results, it is necessary to impose the continuity of the shape functions and their r -derivatives at the interface of the two domains. The r -derivatives are computed with a spectral collocation method, based on the Chebyshev polynomials (Canuto, 1988). In the streamwise direction, a first order backward Euler scheme is used.

As the problem is parabolic, the first step of the procedure is to start with a known solution at $x = x_0$, $\hat{q}(r, x_0)$ and $\alpha(x_0)$. This solution is the result of the linear parallel stability theory at this location. We march then to the next station $x = x_0 + \Delta x$, and, using $\alpha(x_0 + \Delta x) = \alpha(x_0)$ as initial guess, $\hat{q}(r, x_0 + \Delta x)$ is determined by solving Eqn (7). The second step is to compute the new $\alpha(x_0 + \Delta x)$ from the obtained $\hat{q}(r, x_0 + \Delta x)$. Following Herbert & Bertolotti, an iteration strategy is used, based on the normalization given by Eqn (6) :

$$\alpha_{j+1}^{n+1} = \alpha_j^n - \frac{i \int_{\Omega} (\hat{\mathbf{v}}_{j+1}^n)^* (\hat{\mathbf{v}}_{j+1}^n - \hat{\mathbf{v}}_j^n) dr}{\int_{\Omega} |\hat{\mathbf{v}}_{j+1}^n|^2 dr} \quad (13)$$

Here, the subscripts j and $j + 1$ refer to the x_0 and $x_0 + \Delta x$ locations, respectively. n

indicates the iteration step number, $\hat{\mathbf{v}}$ is the vector of velocity shape functions $[\hat{u}_r; \hat{u}_\theta; \hat{u}_x]$, and $\Omega = [0; r_{max}]$ is the radial domain. At each iteration step, the shape functions are computed from Eqn (7), a corresponding new α is computed from Eqn (13), and the procedure continues until the change in α is less than some prescribed value ($\sim 10^{-6}$). In the last step, after the convergence is obtained at this station, we march to the next station, and repeat the whole procedure.

The global PSE system consists in the PSE equation (7), the normalization (6), boundary conditions (10) + (12) and an initial value at $x = x_0$. Equation (7) is parabolic, but to compute the solution the additional normalization equation (6) is needed as explained before. The global system is then nonlinear since normalization (6) is nonlinear. However the global system is still linear with respect to an amplitude fixed by the initial value : if $\hat{\phi}$ is solution, $\alpha\hat{\phi}$ where α is a complex constant is also a solution. But the system is not additive : if $\hat{\phi}_1$ and $\hat{\phi}_2$ are solutions, $\hat{\phi}_1 + \hat{\phi}_2$ is generally not a solution. Besides the mathematical nature of the global PSE approximation is questionable. Haj-Hariri (1994) performed a characteristics analysis of the viscous PSE system that shows weak ellipticity of acoustic origin for $\alpha_r \neq 0$, where α_r is the real part of the complex streamwise wavenumber α . This effect can be alleviated either by dropping the pressure-gradient term $\partial\hat{p}/\partial x$ or by choosing a sufficiently large marching step to skip over the small upstream influence. In the present work the latter solution is used. For marching with simple backward differences, Li & Malik (1996) (see also Andersson et al. (1998) for an extended study of this issue) obtained the limit :

$$\Delta x > 1/\alpha_r \quad (14)$$

This condition implies that a maximum of 2π steps per disturbance wavelength is allowed for the marching. But, as slowly varying shape functions are computed, this step-size restriction does not cause problems about accuracy in the practical cases.

Whatever the choice of step size and normalization, the prediction by the PSE analysis has to be the same, so long as the step size satisfies the stable marching criterion. Figure 1 gives the evolution of the physical value of the fluctuating pressure as function of the axial position x at a fixed radial position $r/D_j = 0.5$, in a test case where the mean flow is hot and has a Mach number of 0.7 (case presented in section 3). The plotted quantity corresponds to the real part of the left hand side of (5) for $m = 0$ and $t = 0$, with a fixed Strouhal number of $St = 0.6$. Three normalizations have been tested ; N_1 corresponds to (6), N_2 is similar to N_1 with in addition the contribution of the pressure and the mass flux, N_3 is a normalization based on the pressure amplitude only. For the second normalization, two different step sizes have been considered. Figure 1 shows the insensitivity of the computation to step sizes and normalizations, which was expected.

For the same mean flow, Figure 2 shows the insensitivity to the choice of the starting location x_0 . The pressure has been normalized so that its maximum value in the plane (r, x) equals 100. Some transients are visible for $r/D_j = 1.5$, but they do not affect significantly the downstream solution. For the jet flows which will be considered in this work, the value $x_0 = 0.3$ is chosen.

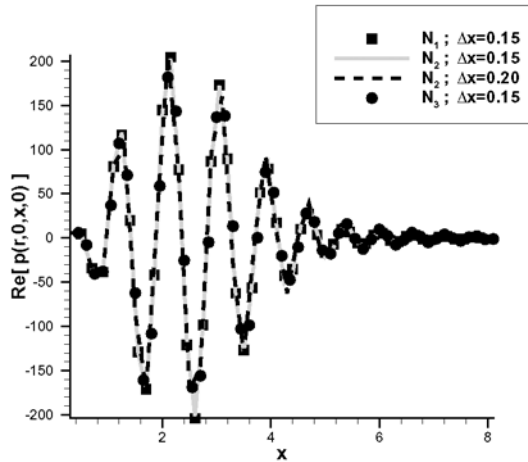


Figure 1. Insensitivity to the choice of normalization and step size in x , $r/D_j = 0.5$, $St = 0.6$, $m = 0$.

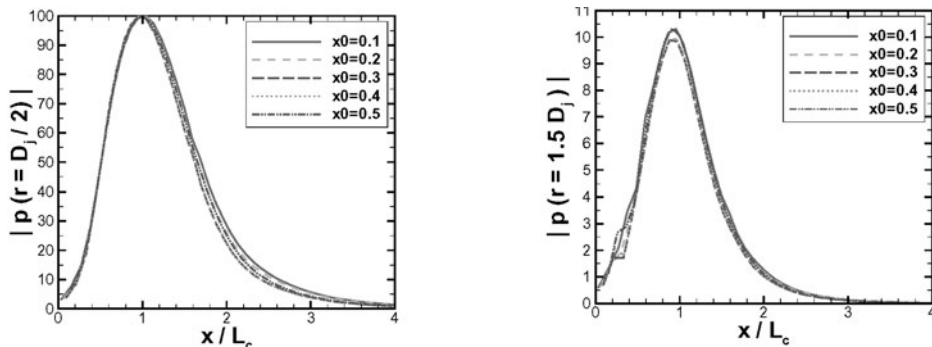


Figure 2. Insensitivity to the choice of the starting location x_0 , for $St = 0.3$ and $m = 0$. Left hand side figure corresponds to $r/D_j = 0.5$, right-hand side figure corresponds to $r/D_j = 1.5$

2.5 Validation

Prior PSE studies of jets (Yen & Messersmith 1998, Balakumar 1998, Malik & Chang 1997, Bertolotti & Colonius 2003, Lin et al. 2004) are based on Navier-Stokes equations. We need first to validate our PSE computations, which are based on Euler equations. Present results are compared with published results of Yen & Messersmith (1998), who have studied an incompressible axisymmetric jet flow, in both viscous and inviscid cases. But even for the inviscid jet flow, their PSE equations are derived from the Navier-Stokes equations. The mean flow is given by:

$$\bar{u}_x(r, x) = \frac{1}{2} \left\{ 1 + \tanh \left[\frac{1}{8} \frac{1}{0.03x + 0.02} \left(\frac{1}{2r} - 2r \right) \right] \right\}$$

$$\bar{\rho}(r, x) = 1$$

The mean radial velocity $\bar{u}_r(r, x)$ is computed from the continuity equation. To simulate an incompressible case, our computations were performed for a Mach number of $M_j = 0.01$. Figure 3 shows the results obtained by Yen & Messersmith (1998) and by the present work. The different values on the x -axis are due to the used reference length, which is R_j (the radius of the jet flow at the exit section) in Yen & Messersmith's paper and $D_j = 2R_j$ in the present approach. The agreement between the two computations is very good, which validates our numerical code in the incompressible case.

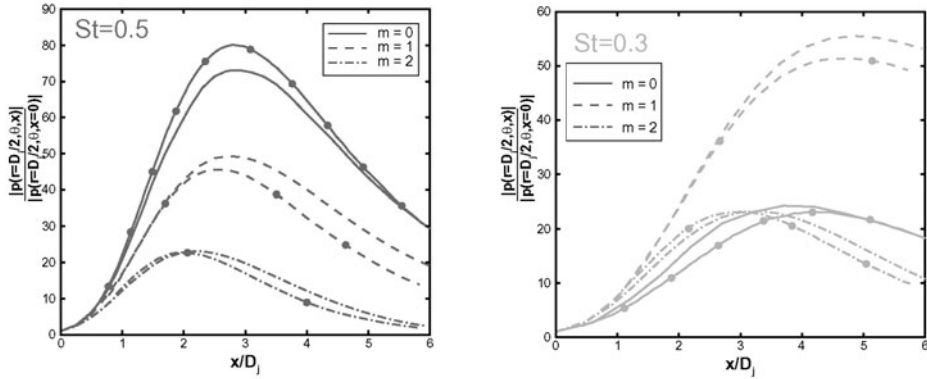


Figure 3. Comparisons between some published (Yen & Messersmith 1998) results (lines + full circles) and the present approach (lines); left hand side figure corresponds to $St = 0.5$, right hand side figure to $St = 0.3$ (here the Strouhal numbers are based on the exit radius, as in Yen & Messersmith (1998)).

To validate the computations in the compressible case, a PSE analysis has been performed for a cold jet ($\bar{\rho}(r, x) = 1$) of Mach number $M_j = 0.8$. The mean streamwise velocity is:

$$\bar{u}_x(r, x) = \frac{1}{2} \left[1 - \tanh \left(\frac{r - 0.5}{b(x)} \right) \right]$$

where $b(x) = \max(0.01; 0.05x)$. The mean flow being very basic, a conventional stability approach (explained in section 2.2) has been easily performed, even in the flow region where the disturbances are damped. The result of this conventional linear stability analysis at the streamwise location $x_0 = 0.3$ was used to initialize the PSE marching procedure. Figure 4 shows the pressure computations for both the conventional and PSE analysis. The agreement between the two analysis is good, with similar trends in the growing and damping of the disturbance. The slight differences may be attributed to the non-parallel effects, which are only considered in the PSE analysis.

A PSE analysis has also been performed for the same mean flow as in Yen & Messersmith (1999). It is a cold supersonic jet flow, the Mach number being $M_j = 2.1$. The stagnation temperature is 294 K, and the Reynolds number is $Re = 70000$. Mean-flow data have been reported by McLaughlin, Seiner & Liu (1980) and Troutt &

McLaughlin (1982). The streamwise evolutions of $h(x)$, $b(x)$ and $u_c(x)$, which are respectively the radius of the core region, the halfwidth of the mixing layer, and the jet centerline velocity, have been computed by the same process as in Yen & Messersmith (1999). The mean flow velocity profiles are then obtained thanks to the empirical formulas used by Tam & Burton (1984) as well as by Yen & Messersmith (1999) and Balakumar (1998) (who also studied the present jet). Figure 5 shows the computed $h(x)$, $b(x)$ and $u_c(x)$. The results of Yen & Messersmith (1999) have been digitized, and the extracted data have been overlayed with the current approach results. The comparison is excellent.

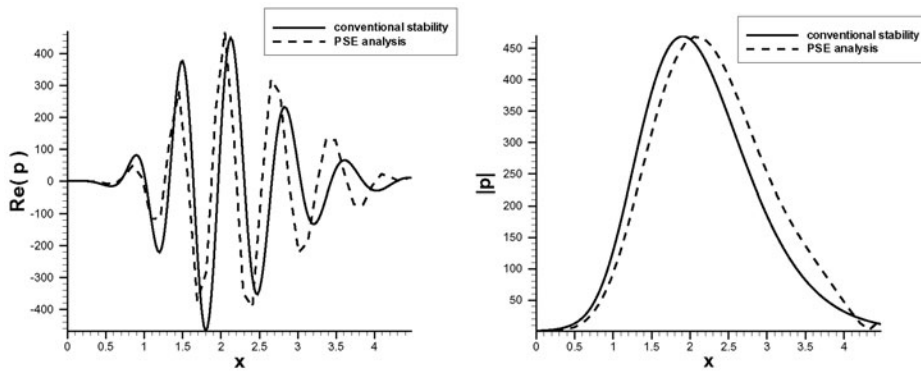


Figure 4. Streamwise variation of the pressure disturbance for conventional stability and PSE solutions

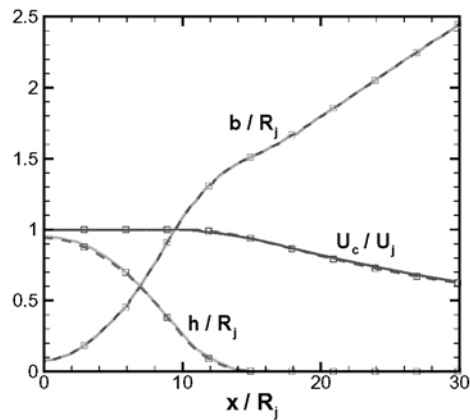


Figure 5. Streamwise variation of h/R_j , b/R_j and u_c/u_j . The Yen & Messersmith (1999) results are plotted in solid lines, our results are plotted in dashed lines with square symbols

The present PSE approach has been then applied on this mean flow. Figure 6 shows the pressure gain over the axial domain along the jet lip line $r/R_j = 1$. Two Strouhal numbers (here based on the jet exit diameter D_j) have been investigated. For each value of St the results computed by the present approach are compared with the results extracted from Yen & Messersmith (1999). The agreement between both methods is reasonably good, which validates the present approach in the supersonic compressible case. However it is important to notice that the present PSE approach is based on the inviscid Euler equations, whereas the Yen & Messersmith (1999) method takes into account the viscous terms. As for this jet the Reynolds number is moderate ($Re = 70000$), neglecting the viscous terms may not be totally justified, which could explain the slight differences between the results. But in the next sections the Reynolds numbers of interest will be much higher (more than half a million), and thus the viscous terms will be negligible.

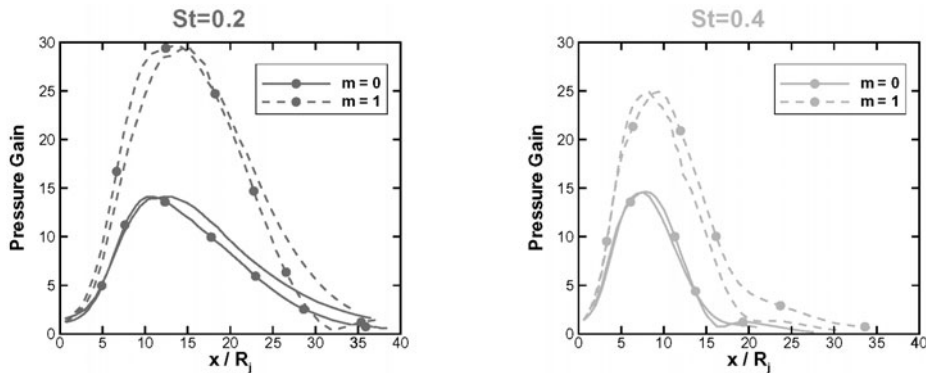


Figure 6. Streamwise variation of pressure gain along $r/R_j = 1$ for two Strouhal numbers and for the two first azimuthal wavenumbers. The Yen & Messersmith (1999) results are plotted in lines with full circles, our results are plotted in lines without symbols

2.6 Wave equation

In the PSE studies based on Navier-Stokes equations (Yen & Messersmith 1998, Balakumar 1998, Malik & Chang 1997, Lin et al. 2004, Bertolotti & Colonius 2003), the PSE equations are parabolized by neglecting the terms in $\partial^2 \hat{q} / \partial x^2$. This means that the desired PSE solution is close to the normal mode form : the x and r coordinates are not treated on an equal footing. As explained by Tam & Burton (1984), it is thus necessary to construct a global solution which consists of both the acoustic and the non-propagating hydrodynamic fluctuation components. That is why Balakumar (1998) or Lin et al. (2004) solve the wave equation to propagate the PSE pressure solution into the far field.

The PSE equations presented in this work are based on the Euler equations, but the boundary conditions are chosen to get a PSE solution which is close to the normal mode form, as explained previously in section 2.3. Therefore to compute the acoustic field,

the method developed by Tam & Burton (1984) and based on the wave equation is used. The near pressure field can be expressed as:

$$p(r, \theta, x, t) = \int_{-\infty}^{+\infty} g(\eta) H_n^{(1)}(i\lambda(\eta)r) e^{i(\eta x + m\theta - \omega t)} d\eta \quad (15)$$

where $\lambda(\eta)$ is the positive square root of $\eta^2 - \rho_\infty M_j^2 \omega^2$ and $g(\eta)$ the wavenumber spectrum, given by:

$$g(\eta) = \frac{1}{2\pi} \int_{-\infty}^{+\infty} \hat{p}_0(x) e^{i \int_{x_0}^x \alpha(\xi) d\xi} e^{-i\eta x} dx \quad (16)$$

Here $\hat{p}_0(x) = \hat{p}(r_0, x)$ is the pressure distribution along the line $r = r_0$ where the mean velocity becomes almost zero. This pressure distribution is a result of the PSE computation.

Not all the near-field pressure fluctuations are radiated into the far field as sound. Following Tam & Burton (1984), a spherical coordinate system (R, χ, ϕ) , centered at the nozzle exit of the jet with the polar axis aligned in the flow direction, is used to find the power of sound emitted. These spherical coordinates are related to the cylindrical coordinates (r, θ, x) by

$$x = R \cos \chi, \quad r = R \sin \chi$$

In the new coordinate system, and for large R , the following far-field pressure is obtained by using the asymptotic form of the Hankel function and the method of stationary phase :

$$\lim_{R \rightarrow +\infty} p(R, \chi, \phi, t) \sim \frac{2}{R} g(\sqrt{\rho_\infty} M_j \omega \cos \chi) e^{i(\sqrt{\rho_\infty} M_j \omega R + m\phi - \omega t - \frac{1}{2}(m+1)\pi)} \quad (17)$$

Therefore the sound power $D(\chi)$ radiated in direction χ per unit solid angle by an excited instability wave is :

$$D(\chi) = \lim_{R \rightarrow +\infty} \frac{1}{2} R^2 |p|^2 = 2 |g(\sqrt{\rho_\infty} M_j \omega \cos \chi)|^2 \quad (18)$$

where $\eta_c = \sqrt{\rho_\infty} M_j \omega$ is the wavenumber associated to the ambient sound speed. The physical interpretation of this wavenumber is that all the waves travelling with a wavenumber smaller than η_c propagate with supersonic phase velocities relative to the ambient sound speed. Only those waves radiate into the far field, the direction of radiation being given by Eqn (18).

3 APPLICATION TO A HOT SUBSONIC FLOW AND COMPARISON WITH LARGE EDDY SIMULATION RESULTS

3.1 Flow configuration

In the present section, a hot subsonic turbulent jet is considered, as previously studied in Piot et al. (2006). The Mach number is $M_j = 0.7$, the ambient temperature and the jet

temperature in the core region are $T_\infty = 280.4$ K and $T_j = 830$ K, respectively. These parameters lead to a large ratio between the outer and inner density : $\rho_\infty/\rho_j = 3$. This jet flow exits from an axisymmetric nozzle of diameter $D_j = 0.08$ m with a velocity $u_j = 410$ m/s. The Reynolds number based on the exit conditions is thus $Re = 4 \times 10^5$.

3.2 Large Eddy Simulation procedure

A Large Eddy Simulation (LES) of the aerodynamic field of the jet is performed without any subgrid model. The MILES (Boris et al. 1992) approach is employed, which means that dissipation is ensured by the numerical scheme. The jet flow is developing freely without any forcing at the inlet boundary condition. The natural instabilities of the flow are excited by the numerical errors only. The present study has been conducted using a second order ADI time scheme and a third order flux splitting spatial scheme. The cartesian grid employed is relatively coarse (1.5 millions cells) and is designed to propagate accurately Strouhal numbers less than $St = 0.3$. This choice of the grid limitation was motivated by the computational limitations and the will to capture the peak of directivity which has been measured experimentally to be around 30 degrees. The acoustic spectrum maximum in this direction was measured to be around $St \approx 0.2$, and this is what the authors wanted to capture when the grid was designed. Therefore the grid limitation of $St \approx 0.3$ should be sufficient to solve qualitatively the noise from the large scale structures. On figure 7, a turbulence spectrum is represented for a location situated near the end of the potential core at $x/D_j \approx 3$ and $r/D_j \approx 0.5$. The $k^{-5/3}$ slope is also plotted. As we can see on this picture, the scheme cut off is not steep at all, it begins to be visible on the amplitude of the spectra around $St \approx 0.5$ and significant only above $St \approx 1$. So the waves with a Strouhal number value above $St = 0.3$ are still present in the computation, but they can undergo phase errors. Thus, some fine scale

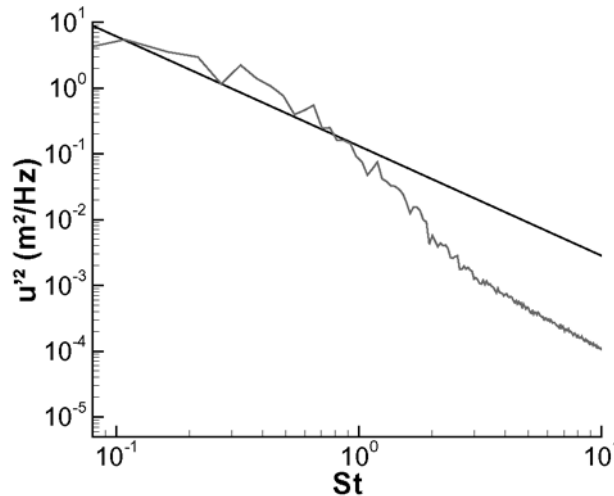


Figure 7. Turbulence spectrum near the end of the potential core (at $x/D_j \approx 3$ and $r/D_j \approx 0.5$) with the $k^{-5/3}$ slope plotted in black.

structures are contained in the LES, but they can undergo dispersion and dissipation errors. When the grid is projected on cylindrical coordinates, the meshing contains 30 points in the radial direction between $r/D_j = 0$ and $r/D_j = 1$, with a refinement around the radial location of the axial velocity inflection point. Between the nozzle and the potential core end $L_c/D_j = 3.3$, there are 65 points in the streamwise direction. The nozzle is included in the computation to avoid special treatments at the inlet boundary condition, but no attempt was made to resolve accurately the boundary layer over the nozzle wall. Non-reflection at the outer boundary conditions is ensured by stretching the grid far from the nozzle. More details about the numerical procedure are available in Lupoglazoff (2002) and Biancherin (Biancherin 2002, 2003).

3.2.1 Governing equations

The compressible Navier-Stokes equations are solved in their conservative form, with a perfect gas assumption. The filtered conservation equations of mass, momentum and total energy per unit volume (hereafter denoted as ρE) are,

$$\frac{\partial \bar{\rho}}{\partial t} + \nabla \cdot (\bar{\rho} \mathbf{u}) = 0 \quad (19)$$

$$\frac{\partial \bar{\rho} \mathbf{u}}{\partial t} + \nabla \cdot (\bar{\rho} \mathbf{u} \otimes \mathbf{u} + \bar{p} \mathbf{I} - \underline{\underline{\tau}}) = 0 \quad (20)$$

$$\frac{\partial \bar{\rho} E}{\partial t} + \nabla \cdot ((\bar{\rho} E + p) \mathbf{u} - \underline{\underline{\tau}} \cdot \mathbf{u} + \underline{\underline{\varphi}}_h) = 0, \quad (21)$$

where the total energy E per unit mass is the sum of internal energy $e(T)$ and kinetic energy $\frac{1}{2} \mathbf{u} \cdot \mathbf{u}$. The filtered total energy per unit volume is $\bar{\rho} E = \bar{\rho} e(T) + \frac{1}{2} \bar{\rho} \mathbf{u} \cdot \mathbf{u}$. Pressure p is related to density ρ and temperature T through the state equation, $p = R\rho T$.

In these filtered Navier-Stokes equations, the dissipative fluxes $\underline{\underline{\tau}}$ and $\underline{\underline{\varphi}}_h$ include subgrid modelization. If $\underline{\underline{S}}_0$ is the deviatoric (trace-free) part of the strain-rate tensor S ,

$$\underline{\underline{S}}_0 = \frac{1}{2} (\underline{\underline{\nabla}} \mathbf{u} + {}^t \underline{\underline{\nabla}} \mathbf{u}) - \frac{1}{3} (\nabla \cdot \mathbf{u}) \mathbf{I}, \quad (22)$$

the expressions for $\underline{\underline{\tau}}$ and $\underline{\underline{\varphi}}_h$ are (neglecting some terms in the development of the filtered quantities),

$$\underline{\underline{\tau}} = 2(\mu + \mu_s) \underline{\underline{S}}_0 \quad (23)$$

$$\underline{\underline{\varphi}}_h = -(\kappa + \kappa_s) \nabla \mathbf{T}. \quad (24)$$

where the dynamic viscosity μ is given by the Sutherland's viscosity law; once μ is known, thermal conductivity κ is determined from the Eucken's relation $\kappa = \mu(c_p + 5r/4)$, with $r = 287.1$ J/(kg K). The specific heat at constant pressure c_p is given by an empirical polynomial function of the temperature.

The type of modelization depends on the expressions used to compute μ_s and κ_s :

- The simplest approach is the Monotonically Integrated Large Eddy Simulation (MILES) (Boris et al. 1992), where the subgrid dissipation comes only from the numerical scheme,

$$\mu_s = 0 \quad , \quad \kappa_s = 0 \quad (25)$$

- In the classical Smagorinsky (1963) model, the expressions for μ_s and κ_s are,

$$\mu_s = \rho(C_s \Delta)^2 \sqrt{2\underline{\underline{S}} : \underline{\underline{S}}} \quad (26)$$

$$\kappa_s = \mu_s c_p / Pr_t \quad (27)$$

where $\underline{\underline{S}} = \frac{1}{2} (\underline{\nabla} \mathbf{u} + {}^t \underline{\nabla} \mathbf{u})$ is the strain-rate tensor, C_s is the Smagorinsky constant (fixed to $C_s = 0.18$) and Pr_t is the turbulent Prandtl number (with the value $Pr_t = 0.9$). Finally Δ represents a norm of the mesh size : $\Delta = \sqrt{\Delta x^2 + \Delta y^2 + \Delta z^2}$, where Δx , Δy , Δz are the step sizes of the cartesian grid.

Both modelizations have been tested and have given very similar results for this jet. So, the MILES approach was chosen for the present study.

3.2.2 Numerical schemes

The temporal integration is based on a three levels scheme, with two parameters θ and χ , developed by Beam and Warming (1978). The quantities \mathbf{q} at time $n+1$ are functions of the same quantities at time n and $n-1$:

$$\begin{aligned} \frac{q^{n+1} - q^n}{\Delta t} = & \left[\frac{\theta}{1+\chi} \frac{\partial q}{\partial t} \right]^{n+1} + \left[\frac{1-\theta}{1+\chi} \frac{\partial q}{\partial t} \right]^n + \frac{\chi}{1+\chi} \left(\frac{q^n - q^{n-1}}{\Delta t} \right) \\ & + \left(\theta - \chi - \frac{1}{2} \right) O(\Delta t) + \left(\theta - \frac{1}{3} \right) O((\Delta t)^2) \end{aligned} \quad (28)$$

A second order implicit ADI (Alternating Direction Implicit) is obtained by taking $\theta = 1$ and $\chi = 0.5$,

$$\frac{3q^{n+1} - 4q^n + q^{n-1}}{2\Delta t} = \left[\frac{\partial q}{\partial t} \right]^{n+1} \quad (29)$$

The spatial scheme belongs to the TVD-MUSCL family and is a third order upwind scheme.

3.2.3 Modal decomposition procedure

The modal analysis of the results provided by the LES is performed by taking the Fourier transform of the pressure field in time and in the azimuthal coordinate. First, the

Fourier transform in the azimuthal coordinate is taken,

$$P_m(x, r, t) = \int_0^{2\pi} p(x, r, \theta, t) e^{-jm\theta} d\theta, \quad (30)$$

second, the Fourier transform in time is taken,

$$P_{m,\omega}(x, r) = \int_0^T P_m(x, r, t) e^{-j\omega t} dt, \quad (31)$$

with $\omega = 2\pi f$ and m the azimuthal mode number. This is the pressure which is used in the comparisons with PSE results.

The data used to compute the Fourier transform are stored with a time resolution of $\Delta t = 45 \times 10^{-6}$ s on a time duration of 72 ms divided into four non overlapping blocks. So the sampling frequency and the frequency resolution of the study are respectively $f_c \approx 22$ kHz and $\Delta f \approx 55$ Hz. There are sixty planes in the azimuthal direction with an angular resolution of $\Delta\theta = 6$ deg., thus only the first 30 modes are accessible, which does not induce a limitation for the following comparisons with the PSE.

3.3 Results and discussion

The mean flow computed by the LES has been used as input for the PSE analysis. Since the LES grid is different *a priori* from the PSE grid, a preliminary work has to be done before the PSE analysis. The following procedure is used. First the \bar{u}_x and $\bar{\rho}$ functions are approximated by analytical functions at each LES grid x values by a standard least square method. The calculated coefficients, which depend on x , are then smoothed by spline routines. The \bar{u}_r function is finally computed by a numerical integration of the continuity equation at each x value of the PSE grid.

PSE calculations have been performed for several Strouhal numbers and azimuthal wavenumbers. However, because of the LES grid construction, the LES results are only accurate for low Strouhal numbers ($St \leq 0.3$). Therefore LES computations results will be presented in this section for two cases $St = 0.2$ and $St = 0.3$ only. In addition, some measurements have been performed on the studied jet flow in CEPRA19 (large facility at ONERA).

Figure 8 shows the streamwise evolution of the fluctuating pressure amplitude at the radial location $r/D_j = 1.5$ for the LES and PSE computations, and for the experiments. The Strouhal number is $St = 0.3$ and the two first azimuthal wavenumbers are considered. The streamwise distance has been scaled by the potential core length, which is $L_c = 3.3D_j$ in the PSE and LES computations. In the experiments, the potential core length is slightly larger. The LES levels have been rescaled to fit with the experimental data by subtracting 8 dB/Hz. As the PSE calculation is based on linear equations, PSE results do not have an intrinsic amplitude. The latter is therefore adjusted at one point to match the LES results amplitude.

We observe that the pressure fluctuations peak at about $x/L_c = 1$, i.e. at the end of the potential core, and decrease further downstream. The LES and PSE computations, and the measurements present the same trend in the growing region, but in the damping region, the PSE results show a larger decrease than the LES ones. Unfortunately, no measurements are available in this region.

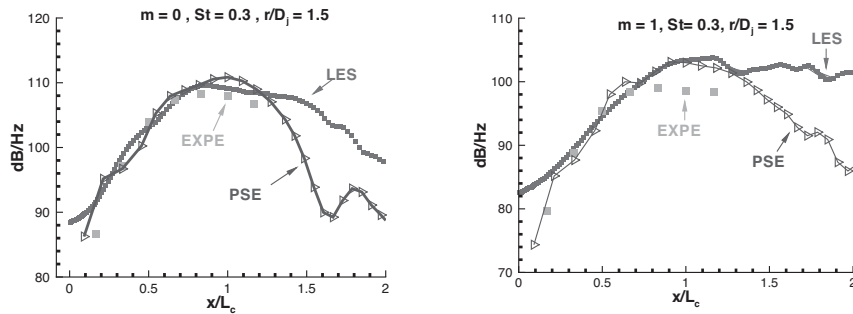


Figure 8. Comparisons between LES (solid lines), experiments (squares) and PSE results (solid lines with triangles) for $St = 0.3$, $r/D_j = 1.5$. Left figure corresponds to the axisymmetric mode: $m = 0$, right hand side to the helical one $m = 1$. The results from the LES are shifted by -8 dB/Hz to match the experimental ones.

Figure 9 shows the same results, but for a Strouhal number $St = 0.2$, and exhibits the same trends, with the peak of pressure fluctuations located here slightly downstream of the potential core end. The agreement between the three kinds of results is here also very good in the growing region. The location of the origin of the dominant pressure fluctuations near the end of the potential core is consistent with previous studies (Balakumar 1998, Malik & Chang 1997, Lin et al. 2004).

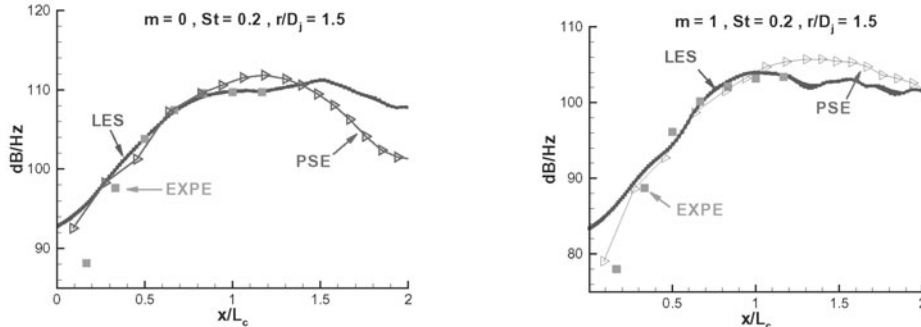


Figure 9. Comparisons between LES (solid lines), experiments (squares) and PSE results (solid lines with triangles) for $St = 0.2$, $r/D_j = 1.5$. Left figure corresponds to the axisymmetric mode : $m = 0$, right hand side to the helical one $m = 1$. The results from the LES are shifted by -8 dB/Hz to match the experimental ones.

Other comparisons between PSE and LES are given in Figures 10 and 11. The fluctuating pressure is here given in the streamwise direction for two radial locations and for the axisymmetric and helical modes. Figure 10 shows the $St = 0.2$ results, Figure 11 the $St = 0.3$ ones. A unique constant has been used to adjust the PSE results ; this means that the reduction observed for $r/D_j = 1.5$ with respect to $r/D_j = 1$ is identically

reproduced by the LES and the PSE approaches. We observe, as explained above, that the PSE damping differs for the LES one at the radial location $r/D_j = 1.5$, whatever the Strouhal number or the azimuthal wavenumber.

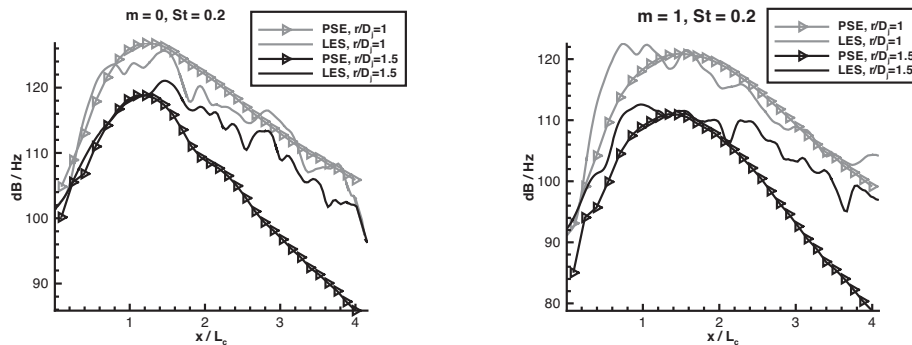


Figure 10. Comparisons between LES and PSE for $St = 0.2$ at two different radial positions. Left figure corresponds to the axisymmetric mode : $m = 0$, right hand side to the helical one $m = 1$.

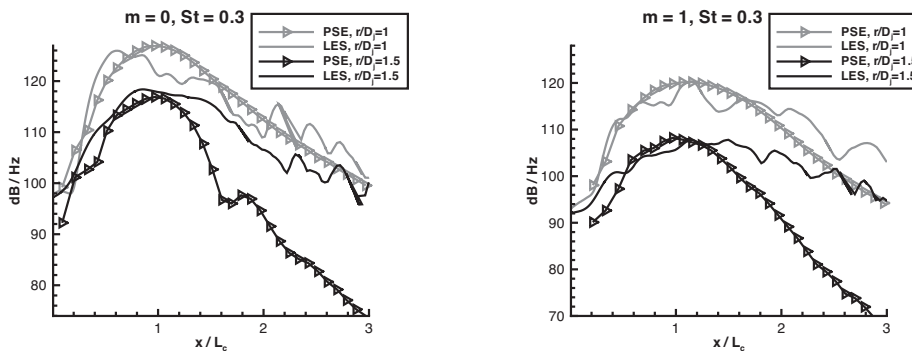


Figure 11. Comparisons between LES and PSE for $St = 0.3$ at two different radial positions. Left figure corresponds to the axisymmetric mode: $m = 0$, right hand side to the helical one $m = 1$.

The acoustic field in the outer part of the jet has been calculated by solving the wave equation, as explained in section 2.6. The lower boundary for the wave equation is located at a radial distance $r_0 = 1.5D_j$, since this is the lowest radial value beyond which the mean flow becomes almost uniform whereas for larger values some numerical uncertainties appear because of the very fast radial decay of the computed PSE pressure fluctuation. But the radiated sound prediction is not satisfactory although the LES, by using a Ffowcs Williams & Hawkings method, predicts sound pressure levels which agree relatively well with the measured ones, as shown in Figure 12. Indeed, in our case, even if the jet is very hot, the instability waves (even amplified for small values of x)

travel almost always subsonically with respect to the ambient sound speed, as shown in Figure 13 for the axisymmetric mode. Similar computations have been performed for higher azimuthal wavenumbers, and it has then been observed that the phase speeds were always subsonic, whatever the streamwise location. Eqn (16) shows that an instability wave has the potential of emitting sound, even if it travels subsonically. But it has been checked numerically that it is not the case for the studied waves, which explains why PSE do not here predict sound radiation.

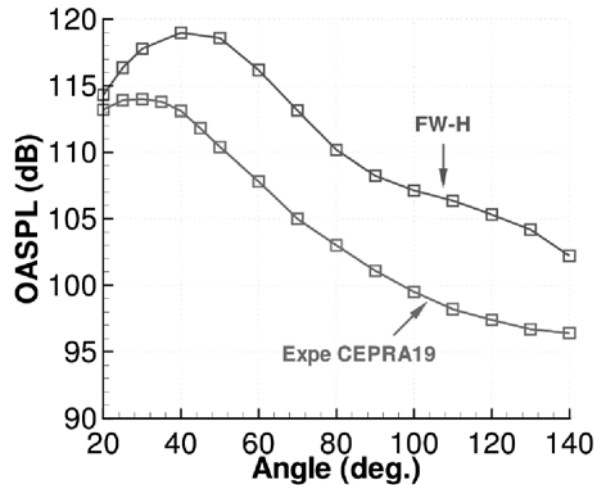


Figure 12. Overall far field sound pressure levels at $75D_j$ from the jet exit. The measurements are plotted in red, the results from the Ffowcs Williams & Hawkins method applied to the LES are plotted in blue

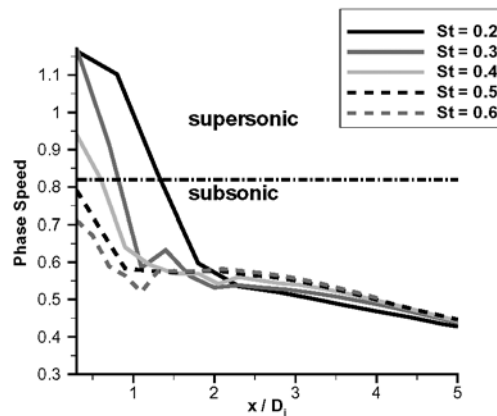


Figure 13. Streamwise evolution of the phase speed ω/α_r for $m = 0$ and for several Strouhal numbers

In a slightly different configuration (a jet flow with a Mach of 0.9 and an exit temperature of 708 K instead of $M_j = 0.7$ and $T_j = 830$ K here), Bertolotti & Colonius (2003) found that sound was not radiated by the shear modes but by what they called core modes. It may be possible that it happens also for the present jet flow, and whereas only the shear modes (Kelvin-Helmholtz modes) have been studied by the PSE analysis, the LES calculation considers also the core modes, and then predicts more sound radiation. But as shown by the previous figures, the fluctuating pressure obtained by the LES around $r/D_j = 1$, $r/D_j = 1.5$, for $St \leq 0.3$ and for $m = 0$ and $m = 1$, is nevertheless very close to the Kelvin-Helmholtz evolution. As previously explained (see section 3.2), the LES grid and the LES model were chosen to capture accurately the fluctuations corresponding to $St \leq 0.3$. However, as shown in Figure 7, fluctuations are still captured more or less accurately up to $St \approx 1$. Figure 12 provides the experimental and LES-computed sound radiation; the latter is obtained from the full fluctuations computed by the LES, without focusing on a specific (St, m) mode. Therefore this sound radiation prediction contains the contribution of both large-scales Kelvin-Helmholtz instabilities and small scales associated to the turbulence. As, according to the PSE analysis, the Kelvin-Helmholtz instabilities do not seem to radiate sound, it may be deduced that in this case the sound radiation is due to the smaller scales. Cheung & Lele (2004) have compared DNS and PSE results for the study of subsonic and supersonic mixing layers, and have also noticed that the majority of the acoustic radiation is not captured by PSE in subsonic mixing layers.

Even if the PSE calculations are not able to correctly capture the acoustic radiation in this case, they still give very interesting results in the near-field of the jet flow. Moreover, they are much faster than the LES calculations: they require less than fifteen minutes on a standard currently available computer to calculate the near-field for a fixed Strouhal number and azimuthal wavenumber.

4 STUDY OF A HOT SUPERSONIC FLOW

4.1 Flow parameters

A hot supersonic jet flow is now considered. A round nozzle of diameter $D_j = 0.09$ m is used. The jet flow exits with a velocity $u_j = 1106$ m/s and a temperature $T_j = 761$ K. The Mach number is then $M_j = 2$ and the ratio between the ambient and the core density is $\rho_\infty/\rho_j = 2.64$. The pressure is, again, assumed to be uniform. The jet is divided into three regions as core, transitional and fully developed regions. In each region, different empirical functions (Tam & Burton 1984, Balakumar 1998) are used to represent the dimensionless mean streamwise velocity profile :

Core region: $0 < x < x_c$

$$\bar{u}_x(r, x) = \begin{cases} 1 & r < h(x) \\ \exp \left[-\ln(2) \left(\frac{r - h(x)}{b(x)} \right)^2 \right] & r \geq h(x) \end{cases} \quad (32)$$

Transition region: $x_c < x < x_f$

$$\bar{u}_x(r, x) = \begin{cases} u_c(x) & r < h(x) \\ u_c(x) \exp \left[-\ln(2) \left(\frac{r - h(x)}{b(x)} \right)^2 \right] & r \geq h(x) \end{cases} \quad (33)$$

Fully developed region: $x > x_f$

$$\bar{u}_x(r, x) = u_c(x) \exp \left[-\ln(2) \left(\frac{r}{b(x)} \right)^2 \right] \quad (34)$$

Here x_c and x_f are the locations of the end of the potential core and of the start of the fully developed region, respectively. In our case, $x_c = 7.6$ and $x_f = 12$. $h(x)$ is the radius of the uniform core region, and is determined by the empirical formula :

$$h(x) = \begin{cases} h_0 \frac{1 - \tanh\left(\frac{0.5}{1-x/x_f}\right)}{1 - \tanh(0.5)} & x < x_f \\ h_0 & x \geq x_f \end{cases} \quad (35)$$

where $h_0 = 0.46363$. $b(x)$ is the half-width of the annular mixing layer and is related to $h(x)$ in such a way that the total axial momentum flux of the jet is constant. The mean density profile is obtained by a Crocco's relation, which gives :

$$\bar{\rho}(r, x) = \left[\bar{u}_x + \frac{1 - \bar{u}_x}{\rho_\infty} + \frac{\gamma - 1}{2} M_j^2 \bar{u}_x (1 - \bar{u}_x) \right]^{-1} \quad (36)$$

The mean radial velocity is computed from the continuity equation.

4.2 Linearized Euler Equations

The present section is concerned with solving the Linearized Euler Equations (LEE), which are more general than the stability-waves equations. The LEE describe both the sound generation and propagation, where the source of sound is represented by a spatially-growing instability wave. This mechanism is the dominant noise source for supersonic jet flows, and one of the first applications of LEE has been proposed by Mankbadi et al. (1998).

The 3-D Euler equations are linearized about the steady mean flow $(\bar{\rho}, \bar{u}_x, \bar{u}_r)$ defined in the previous section to allow comparisons between both LEE simulations and PSE solutions. The spatial derivatives are computed using the eleven-point stencil finite-difference scheme of Bogey & Bailly (2004), the time integration is performed using an optimized explicit six-step low-storage Runge-Kutta algorithm and radiation boundary conditions are implemented. The forcing of the mean flow is obtained by introducing vortical perturbations in the shear-layer (Bogey & Bailly 2005). The fluctuating velocity is modified every time step as follows:

$$\mathbf{u} = \mathbf{u} + \varepsilon \sin(\omega t - m\theta) \mathbf{u}^f$$

where the shape of the forcing reads in cylindrical coordinates :

$$\begin{pmatrix} u_x^f \\ u_r^f \end{pmatrix} = \frac{r_0}{r} \exp \left[-\ln 2 \frac{\Delta^2(x, r)}{\Delta_0} \right] \begin{pmatrix} (r - r_0)/\Delta_0 \\ -(x - x_0)/\Delta_0 \end{pmatrix}$$

with $\Delta^2 = (x - x_0)^2 + (r - r_0)^2$. The forcing is located at (x_0, r_0) , and the chosen numerical parameters are $\Delta_0 = 2\delta_\theta$, $x_0 = 0$, $r_0 = r_j - 2\delta_\theta$, where δ_θ is the momentum thickness at the x_0 location. The computations have been performed with $\varepsilon = 10^{-3}$, and the results presented in the following section have been normalized by ε . This procedure, as well as the numerical algorithm, have been developed for the direct computation of aerodynamic noise (Bogey & Bailly 2006). The computational domain is discretized by a 7.7 millions points Cartesian grid, with 40 points in the initial diameter. The whole domain is about $-2D \leq x \leq 28D$, $-4D \leq y \leq 4D$ and $-4D \leq z \leq 12D$ for the low frequency case $St = 0.3$. The time of the simulation corresponds to 30 periods of the source, and the root mean square fluctuating pressure is calculated over the last four periods. The time step is imposed by the classical CFL condition, yielding $CFL = \Delta t c_0/\Delta y = 1$ in the present case. Note that Δt denotes the time step, c_0 the speed of sound and Δy the transverse step size. The computations are performed on a Nec-Sx5 with a CPU time by time iteration and by mesh point of 5.8×10^{-7} s. As for the PSE approach, each computation corresponds to one value of the Strouhal number and one value of the azimuthal wavenumber.

4.3 Comparison between LEE and PSE results

PSE and LEE computations have been performed for a Strouhal number $St = 0.3$ and for the two first azimuthal wavenumbers. The mean flow, which has been described in the previous section, is analytical. On the contrary to the previous comparisons with LES results, there is therefore no preliminary work to do on the computation grid. The evolution of the disturbances inside the jet is computed using the PSE method, which is initialized by a conventional stability result, as in the previous case of a subsonic jet. The eigenfunction of the most amplified mode is computed with the conventional stability approach. This mode has in this case a supersonic phase speed and is thus expected to radiate sound. On the contrary to the previously studied subsonic jet case, the PSE equations are not parabolic themselves for the considered supersonic hot jet. The parabolicity criterion given in Eqn (9) is indeed not satisfied in the whole computational domain. Nevertheless the computation of the solution seems still possible, provided that the normalization and the marching step size are carefully chosen. The PSE results are then used to compute the acoustic pressure field by solving the wave equation, as explained in section 2.6. The lower boundary for the wave equation is located at a radial distance r_0 of 1.5 diameters of the jet, since the mean flow becomes almost uniform beyond it. The LEE calculations provide directly the acoustic pressure field. As previously explained, the mathematical form (5) for the PSE fluctuations is forced to be close to the normal mode which assumes a weak dependence with respect to x compared to the r -dependence. This difference is not compatible with a sound radiation evaluation. On the opposite the LEE do not assume any scaling: LEE results are global in nature.

To allow a valid comparison, the PSE pressure levels have been matched with the LEE at one arbitrary point, defined by the radial location $r/D_j = 4$ and by the axial location where the pressure reaches its streamwise maximum value. This has been done once for each case of Strouhal number and azimuthal wavenumber since the two predictions methods are linear.

Figures 14 and 15 show the spatial evolution of the acoustic pressure amplitude, for the azimuthal wavenumbers $m = 0$ and $m = 1$, respectively. The left figure displays the LEE computations, the right figure the results obtained by the PSE combined with a wave equation. The plotted pressure levels are the same for both figures, i.e. for both computations and for both wavenumbers. We observe that the noise is radiated in a wedge shaped region. For many supersonic axisymmetric jets, it can be observed that the helical mode radiates more sound than the axisymmetric one. This behaviour can not be checked with either the PSE or LEE approach, as both are linear. However, as the LEE computations have been excited in both cases $m = 0$ and $m = 1$ by the same level of forcing $\varepsilon = 10^{-3}$, figures 14 and 15 show nevertheless that the helical mode reacts more powerfully than the axisymmetric mode. The agreement between the LEE and PSE computations is very good whatever the azimuthal wavenumber: the shape of pressure evolution is the same for both methods, which predict almost exactly the same

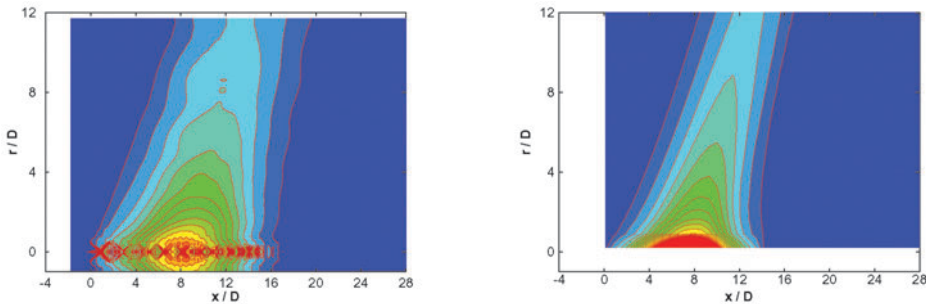


Figure 14. LEE (left figure) and PSE (right figure) spatial evolution of the acoustic pressure amplitude for $St = 0.3$ and $m = 0$

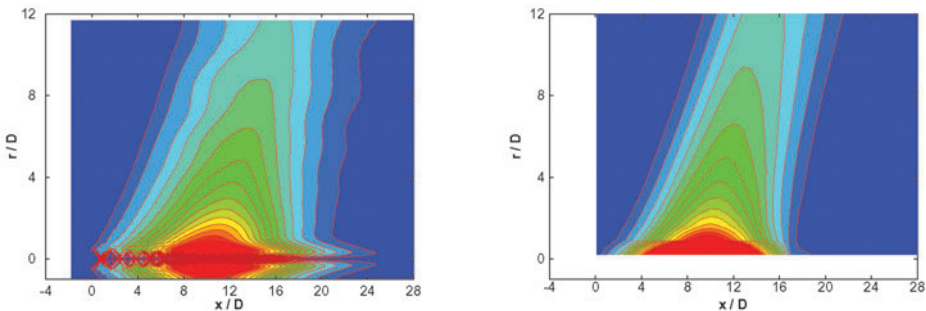


Figure 15. LEE (left figure) and PSE (right figure) spatial evolution of the acoustic pressure amplitude for $St = 0.3$ and $m = 1$

sound radiation angle. Although the PSE pressure levels have been matched with the LEE ones at only one point, we can see that the spatial variation is totally similar for both methods. Moreover, the figures depict that most of the noise is radiated in the region located between the end of the potential core and the beginning of the fully developed region ($x_c = 7.6 < x < x_f = 12$).

To investigate more precisely the agreement between the results of the two methods, Figures 16 and 17 show the evolution of the pressure amplitude with the axial distance for three various radial locations and still for both azimuthal wavenumbers $m = 0$ and $m = 1$. A good agreement between the LEE and PSE results is found, but the PSE method slightly under-predicts the streamwise location of the pressure peak. Moreover the pressure damping is slightly faster in the PSE computations than in the LEE ones. However the decrease in the maximum amplitude value with the radius location is predicted in a similar way by both methods. The agreement between the LEE and PSE predictions of the radial evolution of the pressure amplitude is also good, as shown in the figures 18 and 19. The PSE approach combined with a wave equation can not

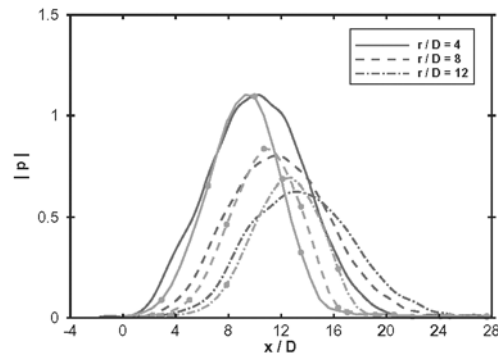


Figure 16. LEE (lines without symbols) and PSE (lines with full circles) streamwise evolution of the acoustic pressure amplitude for $St = 0.3$ and $m = 0$

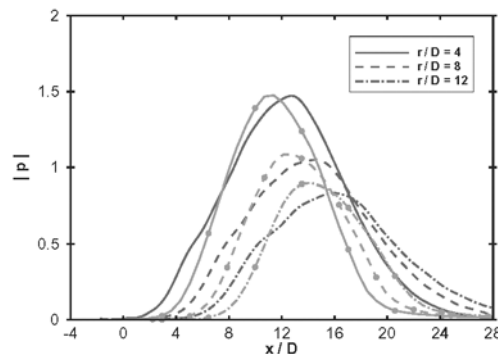


Figure 17. LEE (lines without symbols) and PSE (lines with full circles) streamwise evolution of the acoustic pressure amplitude for $St = 0.3$ and $m = 1$

compute the pressure inside the jet. Thus on Figures 18 and 19 the wave equation pressure profiles have been composited with the direct PSE pressure solutions for radial locations $r < r_0$, which enables to get a continuous graph.

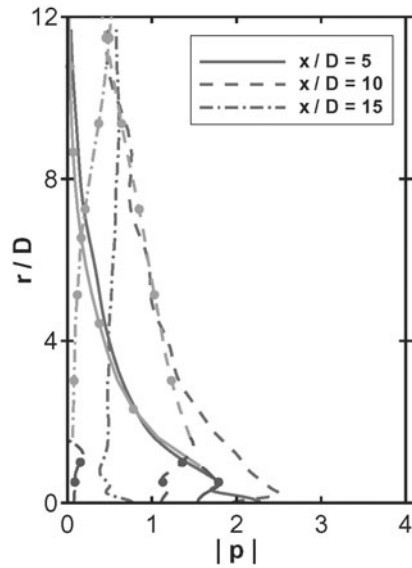


Figure 18. LEE (lines without symbols) and PSE (lines with full circles) radial evolution of the acoustic pressure amplitude for $St = 0.3$ and $m = 0$

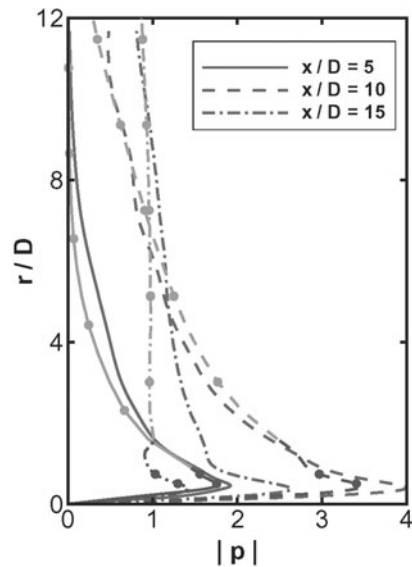


Figure 19. LEE (lines without symbols) and PSE (lines with full circles) radial evolution of the acoustic pressure amplitude for $St = 0.3$ and $m = 1$

To get comparisons inside the jet, PSE results are used directly, without solving the wave equation. Figures 20 and 21 show the evolution of the pressure amplitude with the streamwise distance for the radial locations $r/D_j = 0.5, 0.75, 1$ and 1.5 . We observe the same trends as previously; however the pressure peak location is here predicted by the PSE computations significantly upstream from the one predicted by the LEE computations.

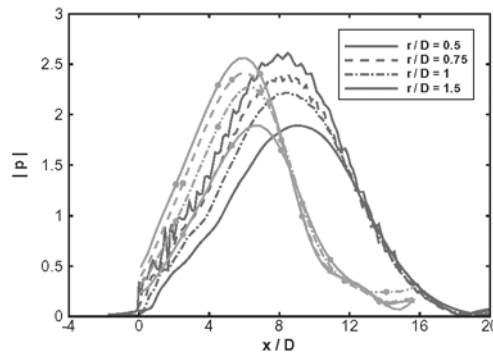


Figure 20. LEE (lines without symbols) and PSE (lines with full circles) streamwise evolution of the pressure amplitude inside the jet for $St = 0.3$ and $m = 0$

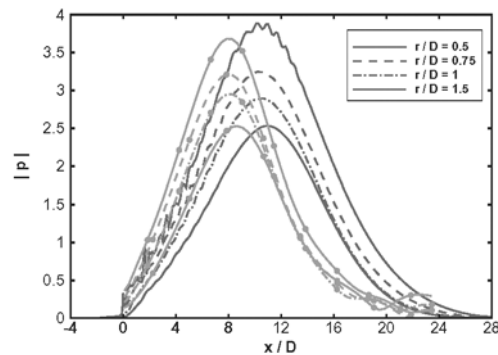


Figure 21. LEE (lines without symbols) and PSE (lines with full circles) streamwise evolution of the pressure amplitude inside the jet for $St = 0.3$ and $m = 1$

LEE and PSE computations have also been performed for the Strouhal number $St = 0.6$. The spatial evolution of the pressure amplitude is shown in Figure 22. The comparison is less good than for $St = 0.3$ because of numerical difficulties in the PSE computations, which create in particular an artificial hump at $x/D_j \sim 14$. But the shape is still similar to the one found by LEE computations. The maximum of sound radiation comes from a region upstream of the one found for $St = 0.3$, which may be explained by the fact that the maximum of instability waves amplitude occurs upstream at $St = 0.6$.

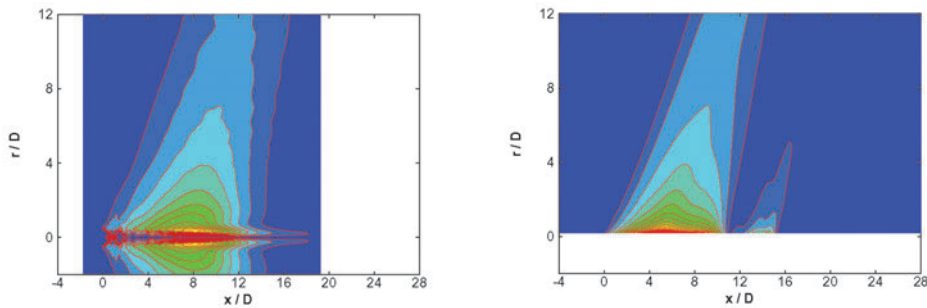


Figure 22. LEE (left figure) and PSE (right figure) spatial evolution of the pressure amplitude for $St = 0.6$ and $m = 1$

4.4 Comparison with conventional stability results

A conventional stability approach has been applied to the studied hot supersonic jet for the helical mode at the Strouhal number $St = 0.3$. The variation of the computed pressure amplitude with the streamwise location is plotted on Figure 23, and is compared to the PSE and LEE results at the radial location $r/D_j = 1$.

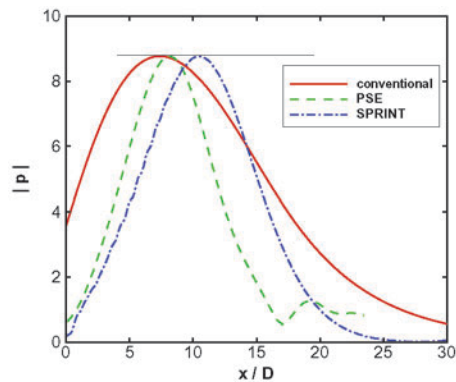


Figure 23. Streamwise evolution of the pressure amplitude for $St = 0.3$ and $m = 1$; in red conventional stability results, in green PSE computations, in blue LEE computations

The conventional stability results differ significantly from the two others ones : the amplification is much weaker and the damping is slower. Moreover, the spatial evolution of the pressure amplitude, computed from the Tam & Burton (1984) approach and shown in Fig 24, is also very different, especially the radiation angle. To explain these differences, note that the conventional stability approach follows the evolution of the Kelvin-Helmholtz mode only whereas the so-called supersonic and subsonic modes also coexist (Tam & Hu 1989) as the flow is supersonic. It may not be the case for the PSE computations : because of the non-linearity of the used normalization, the solution may be a mixing of different modes, and thus follow basically the most amplified combination.

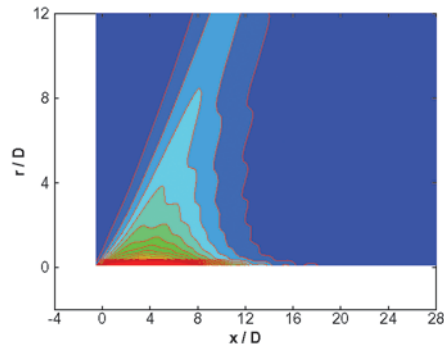


Figure 24. Spatial evolution of the pressure amplitude for $St = 0.3$ and $m = 1$; result from the conventional stability approach

5 CONCLUSIONS

In this work, a Parabolized Stability Equations code based on Euler equations has been developed to study the stability of axisymmetric jets. It has been shown that the Euler-based PSE equations are parabolic rather than parabolized as long as a specific parabolicity criterion is satisfied. However, as in other PSE studies, it is still necessary to use a sufficiently large marching step size to avoid numerical instabilities.

Calculations have been performed for two different jets: a hot subsonic $M_j = 0.7$ jet and a hot supersonic $M_j = 2$ jet. A LES simulation has been applied to the subsonic jet, and some measurements have been made. The mean flow computed by the LES has been used as the base flow of the PSE approach. When compared to the LES simulation and the experiments, PSE method predicts very well the spatial growth of the disturbances. The maximum of pressure disturbance amplitude is reached near the end of the jet potential core. But the spatial damping is overpredicted in the PSE results with respect to the LES simulation. We have also shown that for this particular hot subsonic jet, the jet shear-layer instabilities travel almost always subsonically, and thus do not contribute significantly to the sound radiation process. The noise radiation predicted by the LES simulation may then not be due to the Kelvin-Helmholtz instability waves. Even if the PSE cannot capture in this case the noise radiation, this study demonstrates how successful is the PSE method in the prediction of spatial development of large-scale instabilities in an axisymmetric subsonic jet.

PSE method has been also applied to a hot supersonic jet, and has been compared to LEE computations. There is once again a very good agreement between both predictions of the spatial evolution of the instabilities. However an accurate comparison between both results show that PSE and LEE computations slightly differ in the prediction of the streamwise location of the disturbance pressure maximum. For the studied jet the large-scale instabilities travel supersonically, and thus radiate sound. To compute the acoustic pressure from the PSE results, the wave equation has been solved. The directivity of the radiated sound is captured as well by PSE as by LEE computations. The noise sources seem to be concentrated near the jet potential core end, and the helical mode dominates the acoustic radiation.

This study shows that the PSE stability approach is very efficient to predict the spatial development of jet large-scale instabilities, in both subsonic and supersonic case. Moreover we get accurate pressure eigenfunctions not only in the unstable flow region but also in the stable flow region. PSE computations have also the major advantage to require a low computational cost compared to other techniques as LES or LEE codes. Moreover, even if numerical instabilities may sometimes appear, PSE numerical implementation is relatively easy. It would be very interesting to develop a non-linear PSE code to improve the accuracy of instabilities and noise predictions.

6. ACKNOWLEDGMENTS

The authors would like to thank Jean-Philippe Brazier for his useful insight into the conventional stability technique.

REFERENCES

- Andersson, N., Eroksson, E. and Davidson, L. (2005). "Large-eddy simulation of subsonic turbulent jets and their radiated sound". *AIAA Journal*, Vol. 43, No. 9, pp. 1899–1912.
- Andersson, P., Henningson, D. and Hanifi, A. (1998). "On a stabilization procedure for the parabolic stability equations". *Journal of Engineering Mathematics*, Vol. 33, pp. 311–332.
- Balakumar, P. (1998). "Prediction of supersonic jet noise". *AIAA Paper 98-1057*.
- Beam, R. M. and Warming, R. F. (1978). "An implicit factored scheme for the compressible Navier-Stokes equations by a generalized implicit method". *Journal of Computational Physics*, Vol. 24, No. 3.
- Bertolotti, F. and Colonius, T. (2003). "On the noise generated by convected structures in a Mach 0.9, hot, turbulent jet". In "*AIAA 2003-1062, 41st Aerospace Sciences Meeting and Exhibit*", Reno, Nevada.
- Bertolotti, F., Herbert, T. and Spalart, P. (1992). "Linear and nonlinear stability of the Blasius boundary layer". *Journal of Fluid Mechanics*, Vol. 242, pp. 441–474.
- Biancherin, A. (2003). Simulation aéroacoustique d'un jet chaud subsonique. Ph.D. thesis, Université Paris VI.
- Biancherin, A., Lupoglazoff, N., Vuillot, F. and Rahier, G. (2002). "Comprehensive 3D unsteady simulations of subsonic and supersonic hot jet flow-fields. Part 2: Acoustic analysis". *AIAA Paper 2002-2600*.
- Bogey, C. and Bailly, C. (2004). "A family of low dispersive and low dissipative explicit schemes for noise computation". *Journal of Computational Physics*, Vol. 194, No. 1, pp. 194–214.
- Bogey, C. and Bailly, C. (2005). "Effects of inflow conditions and forcing on subsonic jet flows and noise". *AIAA Journal*, Vol. 43, No. 5, pp. 1000–1007.
- Bogey, C. and Bailly, C. (2006). "Computation of a high Reynolds number jet and its radiated noise using large eddy simulation based on explicit filtering". *Computer & Fluids*, Vol. in press (available online).

- Boris, J., Grinstein, F., Oran, E. and Kolbe, R. (1992). "New insights into Large-Eddy Simulation". *Fluid Dyn. Res.*, Vol. 10, pp. 199–228.
- Canuto, C., Hussaini, M., Quarteroni, A. and Zang, T. (1988). Spectral methods in fluid dynamics. Springer Series in Computational Physics.
- Cheung, L. and Lele, S. (2004). "Acoustic radiation from subsonic and supersonic mixing layers with nonlinear PSE". In "AIAA 2004-363, 42nd Aerospace Sciences Meeting and Exhibit", Reno, Nevada.
- Crighton, D. and Gaster, M. (1976). "Stability of slowly diverging jet flow". *Journal of Fluid Mechanics*, Vol. 77, pp. 397–413.
- Day, M., Mansour, N. and Reynolds, W. (2001). "Nonlinear stability and structure of compressible reacting mixing layers". *Journal of Fluid Mechanics*, Vol. 446, pp. 375–108.
- Haj-Hariri, H. (1994). "Characteristics analysis of the parabolized stability equations". *Stud. Appl. Math.*, Vol. 92, pp. 41–53.
- Herbert, T. (1991). "Boundary-layer transition - analysis and prediction revisited". *AIAA Paper 91-0737*.
- Herbert, T. (1993). "Parabolized stability equations". AGARD-R-793, AGARD-FDP-VKI Special course on Progress in Transition Modelling, VKI, Rhode-Saint-Genese, Belgium.
- Herbert, T. and Bertolotti, F. (1987). "Stability analysis of non-parallel boundary layers". *Bull. Am. Phys. Soc.*, Vol. 32.
- Li, F. and Malik, R. (1996). "On the nature of the PSE approximation". *Theoret. Comput. Fluid Dynamics*, Vol. 8, pp. 253–273.
- Lin, R., Reba, R., Narayanan, S., Hariharan, N. and Bertolotti, F. (2004). "Parabolic stability equation based analysis of noise from an axisymmetric hot jet". In "2004 ASME Heat Transfer/Fluids Engineering Summer Conference", Charlotte, North Carolina.
- Lupoglazoff, N., Biancherin, A., Vuillot, F. and Rahier, G. (2002). "Comprehensive 3D unsteady simulations of subsonic and supersonic hot jet flow-fields. Part 1: Aerodynamic analysis". *AIAA Paper 2002-2599*.
- Malik, M. and Chang, C. (1997). "Nonparallel and nonlinear stability of supersonic jet flow". *Computers and Fluids*, Vol. 29, pp. 327–365.
- Malik, M. and Chang, C. (1997). "PSE applied to supersonic jet instability". In "AIAA 97-0758, 35th Aerospace Sciences Meeting and Exhibit", Reno, Nevada.
- Mankbadi, R., Hixon, R., Shih, S. and Povinelli, L. (1998). "Use of linearized Euler equations for supersonic jet noise prediction". *AIAA Journal*, Vol. 36, No. 2, pp. 140–147.
- McLaughlin, D., Seiner, J. and Liu, H. (1980). "On the noise generated by large scale instabilities in supersonic jets". *AIAA Paper 80-0964*.
- Michalke, A. (1984). "Survey on jet instability theory". *Prog. Aerospace Science*, Vol. 21, pp. 159–199.

- Millet, C. and Casalis, G. (2002). "Selection of acoustic modes in Supersonic Jets". In "8th AIAA/CEAS Aeroacoustics Conference", Breckenridge Colorado.
- Mitchell, B., Lele, S. and Moin, P. (1999). "Direct computation of the sound generated by vortex pairing in an axisymmetric jet". *Journal of Fluid Mechanics*, Vol. 383, pp. 113–142.
- Morris, P. (1981). "Stability of a two-dimensional jet". *AIAA Journal*, Vol. 19, No. 7, pp. 857–862.
- Mosheni, K., Colonius, T. and Freund, J. (2002). "An evaluation of linear instability waves as sources of sound in a supersonic turbulent jet". *Physics of fluids*, Vol. 14, No. 10, pp. 3593–3600.
- Muller, F., Vuillot, F., Rahier, G. and Casalis, G. (2005). "Modal analysis of a subsonic hot jet LES with comparison to the linear stability analysis". In "11th AIAA/CEAS Aeroacoustics Conference", Monterey California.
- Piot, E., Casalis, G. and Muller, F. (2006). "A comparative use of the PSE and LES approaches for jet noise predictions". In "AIAA 2006-2441, 12th AIAA/CEAS Aeroacoustics Conference", Cambridge Massachusetts.
- Saric, W. and Nayfeh, A. (1975). "Non parallel stability of boundary-layer flows". *Physics of Fluids*, Vol. 18, pp. 945–950.
- Smagorinsky, J. (1963). "General circulation experiments with the primitive equations". *Monthly Weather Review*, Vol. 91, No. 3.
- Tam, C. (1995). "Supersonic jet noise". *Annual Review of Fluid Mechanics*, Vol. 27, pp. 17–43.
- Tam, C. and Burton, D. (1984). "Sound generated by instability waves of supersonic flows. Part 2: axisymmetric jets". *Journal of Fluid Mechanics*, Vol. 138, pp. 273–295.
- Tam, C., Golebiowski, M. and Seiner, J. (1996). "On the two components of turbulent mixing noise from supersonic jets". In "11th AIAA/CEAS Aeroacoustics Conferences", State College, PA.
- Tam, C. and Hu, F. (1989). "On the three families of instability waves of high-speed jets". *Journal of Fluid Mechanics*, Vol. 201, pp. 447–483.
- Tam, C. and P.Chen (1994). "Turbulent mixing noise from supersonic jets". *AIAA Journal*, Vol. 32, No. 9, pp. 1774–1780.
- Troutt, T. and McLaughlin, D. (1982). "Experiments on the flow and acoustic properties of a moderate Reynolds-number supersonic jet". *Journal of Fluid Mechanics*, Vol. 116, pp. 123–156.
- Yen, C. and Messersmith, N. (1998). "Application of parabolized stability equations to the prediction of jet instabilities". *AIAA Paper 98-0334*.
- Yen, C. and Messersmith, N. (1999). "The use of compressible parabolized stability equations for prediction of jet instabilities and noise". *AIAA Paper 99-1859*.

APPENDIX: PSE EQUATION

The parabolized stability equation is :

$$\hat{A}\hat{\phi} + \hat{B}\frac{\partial\hat{\phi}}{\partial x} + \hat{C}\frac{\partial\hat{\phi}}{\partial r} = 0 \tag{37}$$

where

$$\hat{A} = \begin{bmatrix} \frac{\partial\bar{\rho}}{\partial r} + \frac{\bar{\rho}}{r} & im\frac{\bar{\rho}}{r} & \frac{\partial\bar{\rho}}{\partial x} + i\alpha\bar{\rho} & -i\omega + \frac{\partial\bar{u}_r}{\partial r} + \frac{\bar{u}_r}{r} + \frac{\partial\bar{u}_x}{\partial x} + i\alpha\bar{u}_x & 0 \\ -i\omega + \frac{\partial\bar{u}_r}{\partial r} + i\alpha\bar{u}_x & 0 & 0 & 0 & 0 \\ 0 & -i\omega + \frac{\bar{u}_r}{r} + i\alpha\bar{u}_x & 0 & 0 & \frac{im}{r\bar{\rho}} \\ \frac{\partial\bar{u}_x}{\partial r} & 0 & -i\omega + \frac{\partial\bar{u}_x}{\partial x} + i\alpha\bar{u}_x & 0 & \frac{i\alpha}{\bar{\rho}} \\ -\frac{1}{\bar{\rho}}\frac{\partial\bar{\rho}}{\partial r} & 0 & -\frac{1}{\bar{\rho}}\frac{\partial\bar{\rho}}{\partial x} & \frac{1}{\bar{\rho}}\left(i\omega - i\alpha\bar{u}_x + \frac{\bar{u}_r}{\bar{\rho}}\frac{\partial\bar{\rho}}{\partial r} + \frac{\bar{u}_x}{\bar{\rho}}\frac{\partial\bar{\rho}}{\partial x}\right) & -M^2(i\omega - i\alpha\bar{u}_x) \end{bmatrix} \tag{38}$$

$$\hat{B} = \begin{bmatrix} 0 & 0 & \bar{\rho} & \bar{u}_x & 0 \\ \bar{u}_x & 0 & 0 & 0 & 0 \\ 0 & \bar{u}_x & 0 & 0 & 0 \\ 0 & 0 & \bar{u}_x & 0 & \frac{1}{\bar{\rho}} \\ 0 & 0 & -\frac{1}{\bar{\rho}}\frac{\partial\bar{\rho}}{\partial x} & -\frac{\bar{u}_x}{\bar{\rho}} & M^2\bar{u}_x \end{bmatrix} \tag{39}$$

$$\hat{C} = \begin{bmatrix} \bar{\rho} & 0 & 0 & \bar{u}_r & 0 \\ \bar{u}_r & 0 & 0 & 0 & \frac{1}{\bar{\rho}} \\ 0 & \bar{u}_r & 0 & 0 & 0 \\ 0 & 0 & \bar{u}_r & 0 & 0 \\ 0 & 0 & 0 & -\frac{\bar{u}_r}{\bar{\rho}} & M^2\bar{u}_r \end{bmatrix} \tag{40}$$

The vector $\hat{\phi}$ is the shape functions vector and is given by :

$$\hat{\phi} = (\hat{u}_r, \hat{u}_\theta, \hat{u}_x, \hat{\rho}, \hat{p})^T. \tag{41}$$

